Visual Analytics of Multidimensional Projections for Constructing Classifier Decision Boundary Maps

Mateus Espadoto[1,2], Francisco Caio M. Rodrigues[1,2] and Alexandru C. Telea[2]

[1]*Institute of Mathematics and Statistics, University of São Paulo*

[2]*Johann Bernoulli Institute, University of Groningen*

{*caiomr, mespadot*}*@ime.usp.br, a.c.telea@rug.nl*

Keywords: Machine Learning, Dimensionality Reduction, Image-Based Visualization

Abstract: Visualizing decision boundaries of modern machine learning classifiers can notably help in classifier design, testing, and fine-tuning. Dense maps are a very recent method that overcomes the key sparsity-related limitation of scatterplots for this task. However, the trustworthiness of dense maps heavily depends on the underlying dimensionality-reduction (DR) techniques they use. We design and perform a detailed study aimed at finding the best DR techniques to use when creating trustworthy dense maps, by studying a large collection of 28 DR algorithms, 4 classifiers, and 2 datasets from a real-world challenging classification problem. Our results show how one can pick suitable DR algorithms to create dense maps that help understanding classifier behavior.

1 INTRODUCTION

Over the last few decades, advances in machine learning (ML) enabled breakthroughs in application areas such as computer vision, natural image processing, path planning, and business intelligence. However, most ML methods work largely as *black boxes*, due to the lack of interpretability behind the decision functions they employ. The more complex such methods become, like in the case of the more recent deep learning (DL) methods, the harder is for their users to understand, customize, and trust them (Ribeiro et al., 2016). As such, recent work has focused on visually explaining how ML techniques learn and take their decisions (Féraud and Clérot, 2002; Rauber et al., 2017b; Rauber et al., 2017a).

One interpretability challenge regards the so-called *decision boundaries* of classifiers. Formally put, let *D* be the data space input by a classifier. The classifier can be seen as a function *f* that assigns a class label to every point in *D*. Understanding how *f*, defined by the training process, partitions *D* into same-class regions, separated by so-called decision boundaries, can help many tasks related to classifier design, *e.g.*, locate how training samples affect the classification of test samples close to them in *D*; spot areas in *D* that require more training samples; and find if the classifier technique used is too 'stiff' to separate complex labeled-sample distributions in *D* (Hamel, 2006; Migut et al., 2015):

Visualizing complex-shaped decision boundaries embedded in a high-dimensional space *D* is very challenging. All existing solutions essentially perform some form of dimensionality reduction (DR) to map *D* to $\mathbb{R}^2$ so as to create directly visible metaphors of the boundaries. However, such solutions have several limitations: Visualizing color-coded scatterplots of training and/or test sets does not actually show the decision *boundaries*, leaving the user to guess where these lie (Rauber et al., 2017b). Image-based dense maps improve upon this by coloring each pixel of the target (screen) image by the assigned label(s) of samples in *D* that project there. Limitations of such solutions include handling only a specific classifier (*e.g.* SVM in (Hamel, 2006)) or using a small-multiple metaphor, which does not scale for high-dimensional spaces *D* (Migut et al., 2015).

A recent attempt to alleviate the above limitations was proposed by (Rodrigues et al., 2018). The key asset of this method is that it creates dense boundary maps for *any* classifier in a generic manner. To do this, however, a 'suitable' DR method needs to be chosen so as to project *D* to $\mathbb{R}^2$. However, it is well known that different DR methods create widely different projections for the same input data (Nonato and Aupetit, 2018; van der Maaten and Postma, 2009; Sorzano et al., 2014). Hence, the displayed dense maps depend on the *combination* of the classifier being studied and the DR method being used to project data. However, (Rodrigues et al., 2018) only tangentially touch such aspects, as they study only the use of t-SNE (van der Maaten and Hinton, 2008) and LAMP (Joia et al., 2011) DR techniques for four classifiers: k-Nearest Neighbors (k-NN), Support Vector Machines (SVM), Logistic Regression (LR), and Convolutional Neural Networks (CNN).

In this paper, we aim to methodically cover the areas left open in (Rodrigues et al., 2018) regarding the choice

of a suitable DR technique. Specifically, we address the following questions:

- How do the depicted decision boundaries differ as a function of the chosen DR technique?
- Which DR techniques are best for a trustworthy depiction of decision boundaries?
- How do misclassifications affect a classifier's decision boundaries?

To answer these questions, we proceed as follows. Section 2 overviews related work and the dense map technique in (Rodrigues et al., 2018). Section 3 presents the experimental setup we used to study how dense maps depend on DR techniques and classifiers, covering a combination of 28 DR techniques and 4 classifiers. Section 4 presents and discusses our results. Section 6 concludes the paper.

2 BACKGROUND

2.1 Preliminaries

We first introduce a few notations. Let $\mathbf{x} = (x^1, \ldots, x^n)$, $x^i \in \mathbb{R}, 1 \leq i \leq n$ be a n-dimensional (nD) real-valued observation or sample, and let $S = \{\mathbf{x}_i\}$, $1 \leq i \leq N$ be a *dataset* of N such samples. Let $\mathbf{x}^j = (x_1^j, \ldots, x_N^j)$, $1 \leq j \leq n$ be the jth feature vector of S. Thus, S can be seen as a table with N rows (samples) and n columns (dimensions). As outlined in Sec. 1, S is sampled from a particular universe, or subspace, $D \subset \mathbb{R}^n$, *e.g.*, the space of all images of digits (LeCun and Cortes, 2018). A *classifier* for D is a function $f : D \to C$ which associates to every $\mathbf{x} \in D$ a class label from a categorical domain C, *e.g.*, the digits 0 to 9. The function f is constructed via a so-called training-set $S_t = \{\mathbf{x}_i, c_i\} | \mathbf{x}_i \in D, c_i \in C$ and tested via a similar, but disjoint, test set S_T. Different machine learning (ML) techniques exist to construct f, some of the best known being Support Vector Machines (SVM), k-Nearest Neighbors (k-NN), Logistic Regression (LR), Random Forests (RF), and Convolutional Neural Networks (CNN) (Krizhevsky et al., 2012).

Exploring how well f was learned from S_t is most typically done by considering all points $\mathbf{x} \in S_T$ labeled by their inferred classes $f(\mathbf{x})$. To visualize these, one typically constructs a scatterplot using *projections* or dimensionality reduction (DR) methods (Hoffman and Grinstein, 2002; Liu et al., 2015). A projection is a function $P : D \to \mathbb{R}^m$, where typically $m = 2$, which aims to preserve data similarities or neighborhoods. That is, if two points $\mathbf{x} \in D$, $\mathbf{y} \in D$ are seen to be similar (by any application-dependent suitable metric, *e.g.* Euclidean distance, cosine distance, or neighborhood rank), then their projections $P(\mathbf{x})$ and $P(\mathbf{y})$ will be close in the target 2D (image) space.

2.2 Decision Boundary Maps

Visualizing the behavior of a classifier via the scatterplot $P(\mathbf{x}) | \mathbf{x} \in S_T$ color-coded by the labels $f(\mathbf{x}) | \mathbf{x} \in S_T$ exploits the power of projections to *group* similar samples $\mathbf{x}$ into clusters in the scatterplot. If such a cluster is uniformly colored, it means that all its underlying (similar) samples were assigned to the same class by the classifier f. Conversely, differently colored 'outlier' points in a cluster typically indicate classification problems. While useful and simple to construct, such scatterplots have the fundamental limitation that they do not show how the classifier treats the *entire* universe D, but only a sparse sampling S_T thereof. Simply put, we do not know what happens in the blank space *between* the scatterplot points.

Recently, (Rodrigues et al., 2018) aimed to overcome this issue by proposing so-called decision-boundary maps. In brief, this method works as follows (see also Fig. 1a): For every pixel $\mathbf{y}$ of the target (projection) space, data samples $\mathbf{x} \in D$ are created, by gathering the Y scatterplot points $P(\mathbf{x})$ that project into $\mathbf{y}$ and, if this number is below a user-prescribed value U, adding $U - Y$ synthetically created points $P^{-1}(\mathbf{y}')$, where $\mathbf{y}'$ are random points falling in the pixel $\mathbf{y}$. Here, $P^{-1} : \mathbb{R}^2 \to D$ is a so-called inverse projection technique that outputs a nD data point given a projected (2D) point. Having now $R = \max(U, Y)$ data samples $\mathbf{x}_1, \ldots, \mathbf{x}_R$ for each image pixel, the respective pixel is colored to reflect their assigned labels $L = \{f(\mathbf{x}_1), \ldots, f(\mathbf{x}_R)\}$. For this, a HSV color is synthesized where hue (H) reflects the most frequent label in L; saturation (S) is high when most labels in L are identical and low (gray colors) when many different labels exist in L; and value (V) encodes the sample point density R (pixels with many samples get brighter).

The key advantages of this method are that it is independent on the classifier technique f being studied; it has no complex-to-set free parameters; but most importantly, it creates *dense maps* where each image pixel is colored to reflect how f behaves for the nD point(s) that map there via the projection P. These effectively partition the image space into several same-color zones, indicating subspaces in D where the classifier behaves identically, *i.e.*, reflect the underlying so-called contiguity hypothesis typical in many ML contexts (Manning et al., 2008). Zone boundaries effectively indicate decision boundaries where the classifier changes the assigned class. Few compact zones with simple (smooth) boundaries indicate that the classifier has little difficulty in taking decisions over D. Multiple disjoint same-color zones and/or zones with tortuous boundaries indicate the opposite. Small-size 'islands' of one color embedded in large zones of different colors suggest misclassifications and/or training problems.
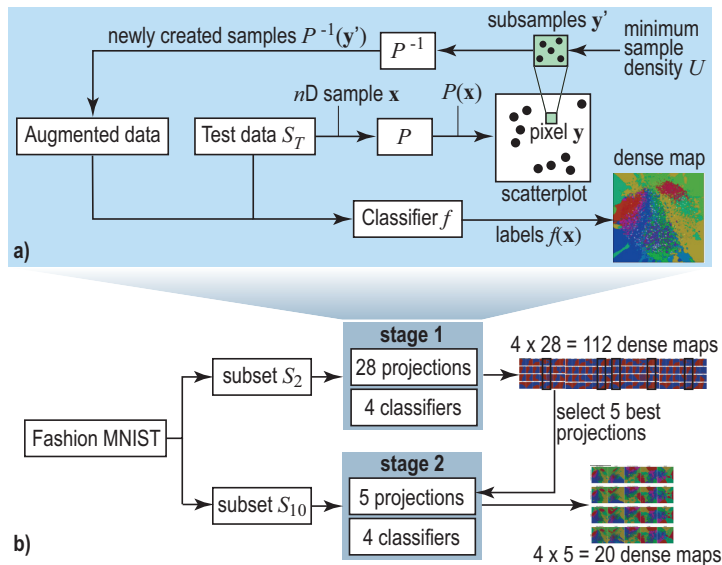
Figure 1: (a) Dense map construction algorithm; (b) Two-phase experiment set-up.

3 EXPERIMENT SETUP

However, the trustworthiness of the dense map technique in (Rodrigues et al., 2018) *heavily* depends on the direct (P) and inverse (P^{-1}) projection techniques it uses. Consider, for example, a toy two-class k-NN classifier for a 3D data space $D \subset \mathbb{R}^3$ trained with a simple S_t consisting of one sample of each class. We know in this case that the decision boundary should be a plane halfway the two training samples. So, a good 2D projection P should ideally render two compact decision zones separated by a straight line. Conversely, a poor P may create several same-class zones having complex curved boundaries; if we saw such an image, we would wrongly judge the behavior of the classifier.

The original proposal used t-SNE (van der Maaten and Hinton, 2008) and LAMP (Joia et al., 2011) to implement P and iLAMP (Amorim et al., 2012) for P^{-1}, respectively. However, tens of other projection techniques exist – for recent surveys, see (Nonato and Aupetit, 2018; van der Maaten and Postma, 2009; Sorzano et al., 2014). To study which of these techniques are most suitable for constructing effective dense maps, we designed and executed a two-stage experiment, as follows (see also Fig. 1b).

Data: We select two different subsets of the Fashion MNIST (Xiao et al., 2017), a state-of-the-art ML benchmark with clothing and accessory images, which supersedes complexity-wise the traditional MNIST dataset (LeCun and Cortes, 2018). Both MNIST and Fashion MNIST have 70*K* grayscale images of 28×28 pixels, split into a training set (60*K* samples) and a test set (10*K* samples). The two subsets are as follows:

- S_2: A two-class subset (classes *T-Shirt* and *Ankle Boot*) that we hand-picked to be linearly-separable;

- S_{10}: An all-class subset (*T-Shirt*, *Trouser*, *Pullover*, *Dress*, *Coat*, *Sandal*, *Shirt*, *Sneaker*, *Bag*, and *Ankle Boot*). This is a non-linearly-separable dataset.

Classifiers: We consider the same classifiers as in (Rodrigues et al., 2018): LR, RF, k-NN (implemented in *scikit-learn*, using their toolkit's default parameters), and CNN (implemented in *keras*). For CNN, we used two convolutional layers with 64 filters each and 3×3 kernels, followed by one 4096-element fully-connected layer, trained with the Adam optimizer (Kingma and Ba, 2014). These classifiers create very different decision boundaries: At one extreme, LR boundaries are linear (hyperplanes). k-NN boundaries are piecewise-linear (facets of *n*D convex polyhedra). RF creates typically more complex boundaries than k-NN. At the other extreme, CNN boundaries can have arbitrarily complex topologies and geometries, due to the complex decision function f coded by the deep network structure. However, CNNs are known to perform very well for classifying images like our dataset, while at the other extreme simple classifiers like LR are highly challenged by such data.

Table 1: Accuracy of classifiers, 2-class and 10-class problems.

Classifier technique	2-class	10-class
Logistic Regression (LR)	1.0000	
Random Forest (RF)	1.0000	0.8332
k-Nearest Neighbors (KNN)	0.9992	0.8613
Conv. Neural Network (CNN)	1.0000	0.9080

Training: The four classifiers were separately trained on the two subsets S_2 ($S_t = 2160$ samples, $S_T = 240$ samples) and S_{10} ($S_t = 10800$ samples, $S_T = 1200$ samples). We verified that the training yielded good accuracies in all cases and especially high ones for the two-problem case. (Tab. 1). This is essential to know when we next
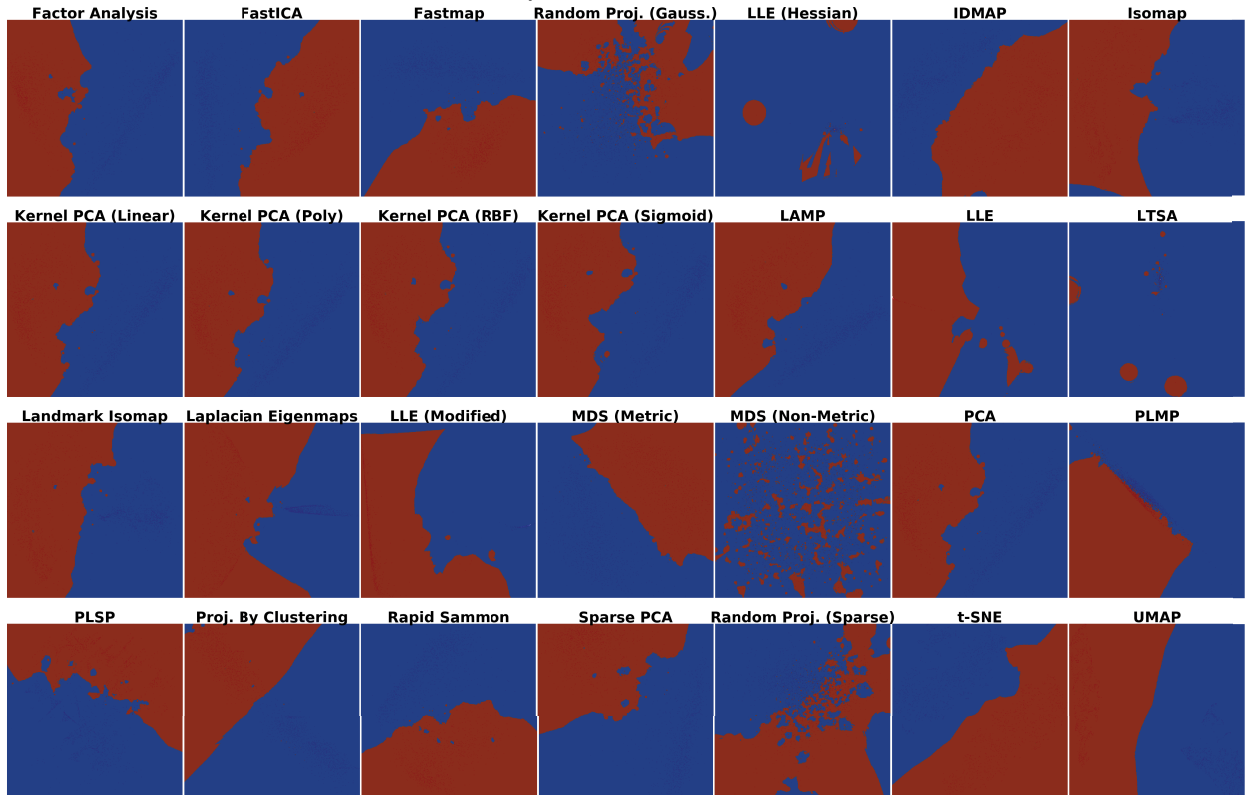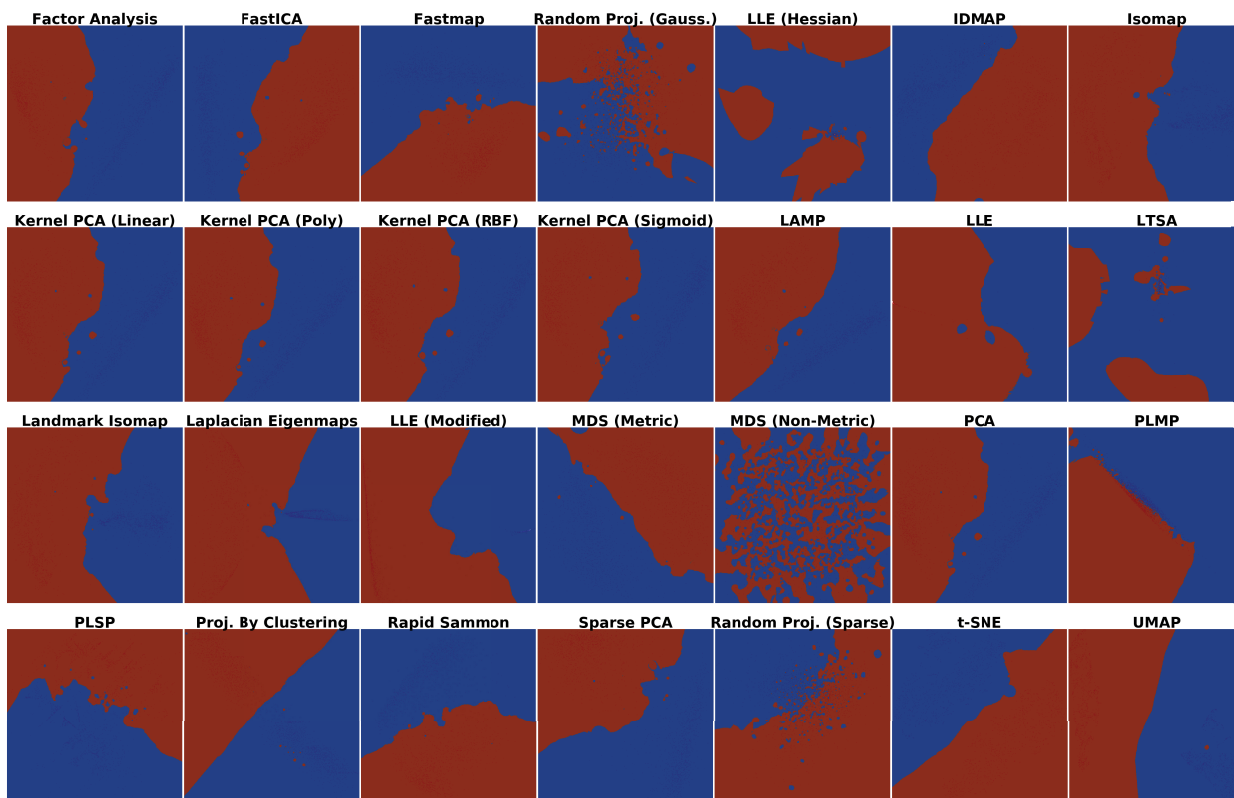
a) Logistic Regression
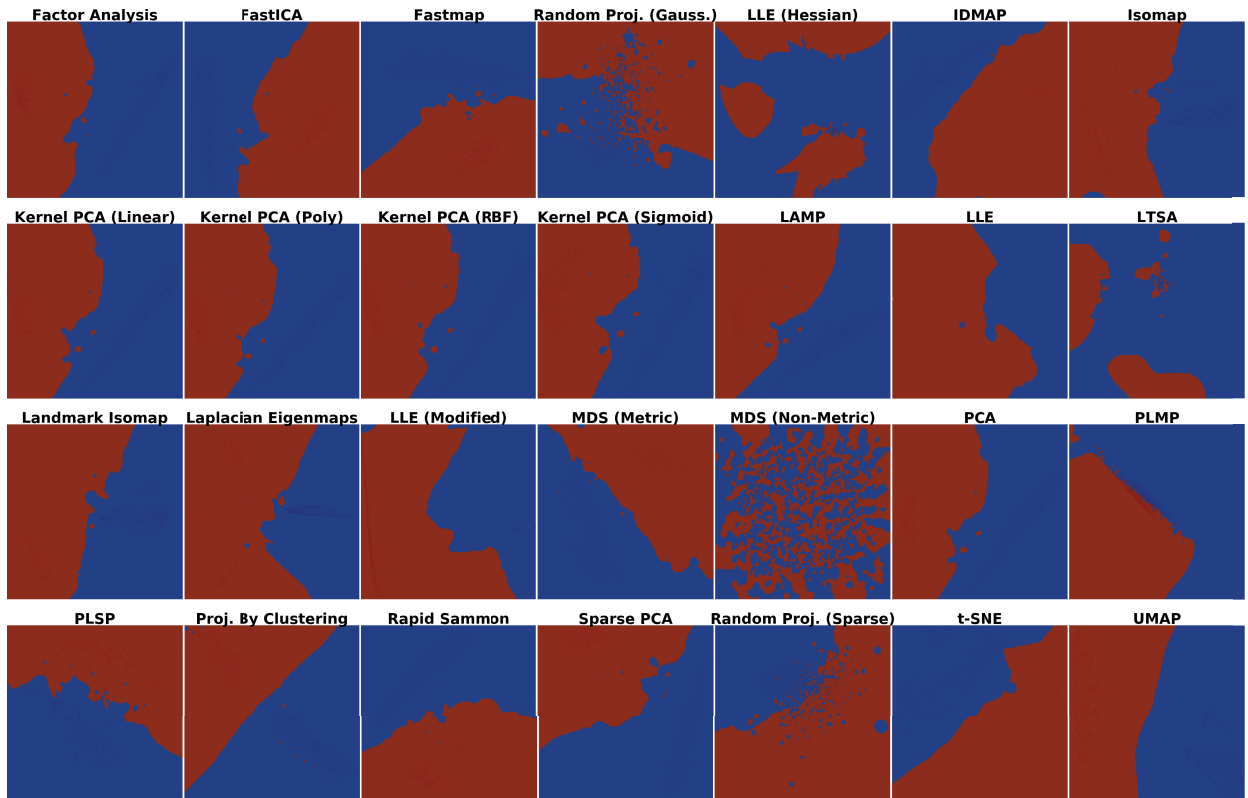
b) Random Forest

Figure 2: Dense maps for Logistic Regression (a) classifier and Random Forest (b) classifiers on the 2-class dataset, all projections.

a) k Nearest Neighbors

Factor Analysis	FastICA	Fastmap	Random Proj. (Gauss.)	LLE (Hessian)	IDMAP	Isomap

Kernel PCA (Linear)	Kernel PCA (Poly)	Kernel PCA (RBF)	Kernel PCA (Sigmoid)	LAMP	LLE	LTSA

Landmark Isomap	Laplacian Eigenmaps	LLE (Modified)	MDS (Metric)	MDS (Non-Metric)	PCA	PLMP

PLSP	Proj. By Clustering	Rapid Sammon	Sparse PCA	Random Proj. (Sparse)	t-SNE	UMAP

b) Convolutional Neural Network

Factor Analysis	FastICA	Fastmap	Random Proj. (Gauss.)	LLE (Hessian)	IDMAP	Isomap

Kernel PCA (Linear)	Kernel PCA (Poly)	Kernel PCA (RBF)	Kernel PCA (Sigmoid)	LAMP	LLE	LTSA

Landmark Isomap	Laplacian Eigenmaps	LLE (Modified)	MDS (Metric)	MDS (Non-Metric)	PCA	PLMP

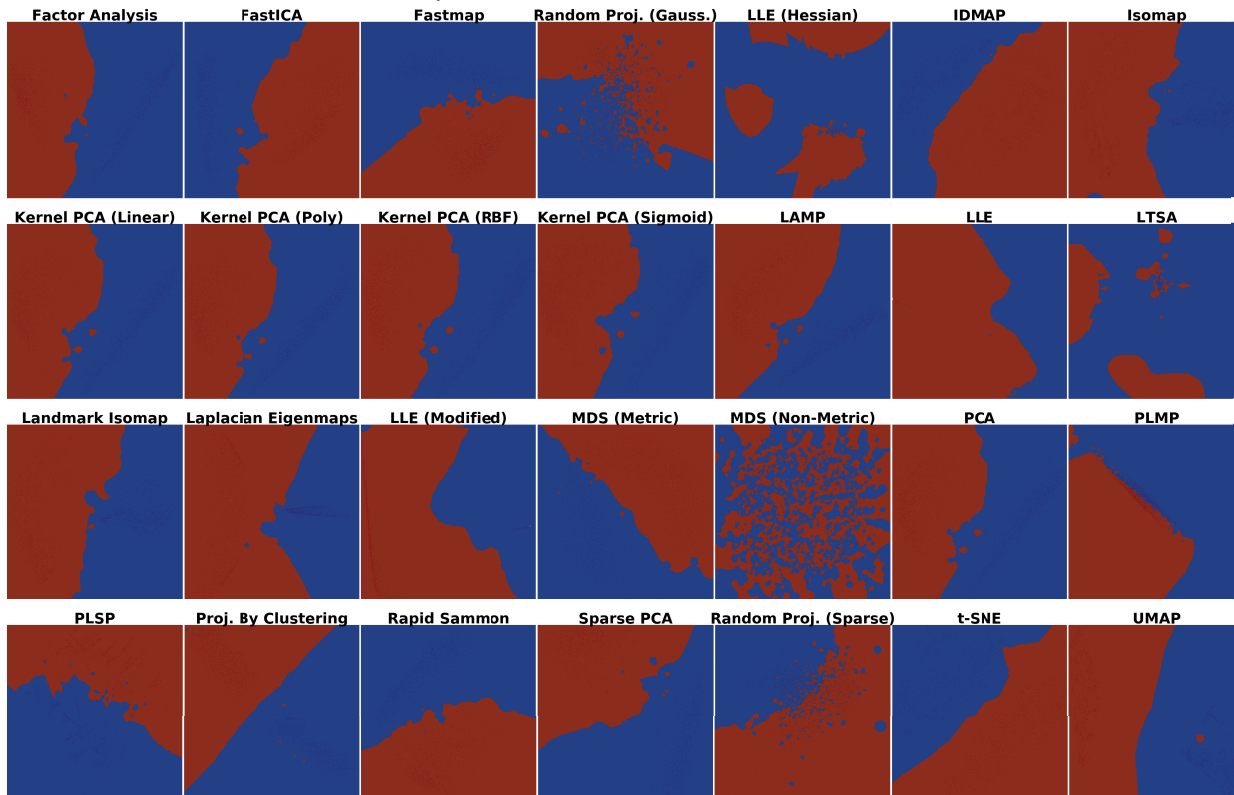| PLSP	Proj. By Clustering	Rapid Sammon	Sparse PCA	Random Proj. (Sparse)	t-SNE	UMAP

Figure 3: Dense maps for k-NN (a) and CNN (b) classifiers on the 2-class dataset, all projections.

gauge the dense maps' ability to capture a classifier behavior (see stage 1 below).

Projections: We selected 28 projection techniques (P) to create dense maps (Table 2). As selection criteria, we considered well-known projections of high quality (following a recent survey (Nonato and Aupetit, 2018)), good computational scalability, ease of use (P should come with well-documented parameter presets), and publicly available implementation. Table 3 lists the parameter settings (default indicates using the standard ones the algorithms come with).

Dense maps: We use a two-stage creation and analysis of dense maps, as follows (Fig. 1b). In stage 1, for S_2, we create dense maps using all 28 projections for all 4 classifiers, yielding a total of 112 dense maps. All maps have a 400×400 pixel resolution. Since S_2 is quite simple (two linearly separable classes), *and* all classifiers for S_2 have very high accuracies (Tab. 1), the resulting maps should display (ideally) two compact zones separated by a smooth, ideally linear, boundary. We visually verify which of the 112 maps best comply with these criteria, and next select the five projections (of the 28 tested ones) which realize these maps. These are shown in bold in Tab. 2. Next, in step 2 of the study, we create dense maps, for all 4 classifiers again, but using the more complex S_{10} dataset. Finally, we explore these visually to gain fine-grained insights allowing us to further comment on the dense-map suitability of the five hand-picked projections.

Table 2: Selected Multidimensional Projections.

Factor Analysis (Jolliffe, 1986)
FastICA (Hyvarinen, 1999)
Fastmap (Faloutsos and Lin, 1995)
IDMAP (Minghim et al., 2006)
Isomap (Tenenbaum et al., 2000)
Kernel PCA (Linear) (Schölkopf et al., 1997)
Kernel PCA (Polynomial)
Kernel PCA (RBF)
Kernel PCA (Sigmoid)
LAMP (Joia et al., 2011)
Landmark Isomap (Chen et al., 2006)
Laplacian Eigenmaps (Belkin and Niyogi, 2002)
LLE (Roweis and Saul, 2000)
LLE (Hessian) (Donoho and Grimes, 2003)
LLE (Modified) (Zhang and Wang, 2007)
LTSA (Zhang and Zha, 2004)
MDS (Metric) (Kruskal, 1964)
MDS (Non-Metric)
PCA (Jolliffe, 1986)
PLMP (Paulovich et al., 2010)
PLSP (Paulovich et al., 2011)
Projection By Clustering (Paulovich and Minghim, 2006)
Random Projection (Gaussian) (Dasgupta, 2000)
Random Projection (Sparse) (Dasgupta, 2000)
Rapid Sammon (Pekalska et al., 1999)
Sparse PCA (Zou et al., 2006)
t-SNE (van der Maaten and Hinton, 2008)
UMAP (McInnes and Healy, 2018)

4 RESULT ANALYSIS

We next discuss the results and insights obtained in our two-stage experiment.

4.1 Phase 1: Picking the best projections

For the simple 2-class problem S_2, all four classifiers yield almost perfect accuracy (Tab. 1). Hence, their decision boundaries are 'where they should be', *i.e.*, perfectly separating the two classes in S_2. Moreover, since S_2 is by construction linearly separable, this means that its dense maps, constructed for these classifiers, should clearly show two compact zones separated by a smooth, simple, boundary. We use this as a visual criterion to rank how well projection techniques can achieve this. Figures 2 and 3 show the dense maps for all 28 tested projections for the four tested classifiers, where red and blue indicate pixels mapping samples having been assigned one of the two labels in S_2. Very interestingly, we see that even for this *very simple* problem not all projections perform the same. Our key observations are as follows:

Stability: The dense maps are surprisingly stable for the same projection over all four classifiers, except for LLA, LTSA, Random Projection (Gaussian), and Random Projection (Sparse). Hence, we already flag these four projections as less suitable.

Smoothness: All projections have relatively smooth boundaries, except Random Projection (Gaussian), Random Projection (Sparse), and MDS (Non-Metric). Since we expect smooth boundaries, these projections are less suitable. The projections which yield boundaries closest on average to a straight line (which is what we expect) are MDS, UMAP, Projection by Clustering, t-SNE, and PLMP.

Compactness: Projections succeed up to widely different degrees in creating two compact, genus-zero, decision zones. t-SNE, UMAP, Projection by Clustering, and IDMAP do this almost perfectly. MDS (Non-Metric), the two Random Projections, LLE (Hessian), and LTSA perform the worst.

Summarizing the above, we select MDS (Metric), PLMP, Projection by Clustering, UMAP, and t-SNE as the overall best projections to analyze further.

4.2 Phase 2: Refined insights on complex data

We now examine how the five selected projections (in phase 1) perform on the 10-class dataset S_{10} which is a tough classification problem (Xiao et al., 2017). We already see this in the lower achieved accuracies (Tab. 1). Hence, we expect to have significantly more complex boundaries. Figure 4, that shows the dense maps for our 4 classifiers for the 5 selected projections, confirms this. Several interesting patterns are visible, as follows.

For a given projection, the dense map patterns are quite similar over all four tested classifiers. This is correct, since the dense map is constructed based on the scatterplot created by that projection from the test set S_T, which is fixed. The variations seen along a given column in Fig. 4 are thus precisely those capturing the differences of decision boundaries due to different classifiers. We see, for instance, that LR tends to create slightly simpler boundaries than the other three classifiers. Conversely, if we scan Fig. 4 row-wise, we see greater variations, which can be purely ascribed to the projection characteristics. Techniques designed to better separate data clusters, such as t-SNE and UMAP, show more compact decision zones with simpler boundaries than MDS, PLMP, and Projection by Clustering. Also, the choice of neighborhood used internally by the projection technique to estimate points in the lower dimension (2D) does not seem to play a key influence: MDS, which uses global neighborhoods, shows similar pattern-variations along classifiers to the other four projections, all of which use local neighborhoods.

Another salient visual element of the dense maps in Fig. 4 is the presence of many small color islands. Let us analyze these in more detail. An island essentially indicates that (at least) one sample was assigned a label different from the labels of most samples that are close to it *in the 2D space*. In turn, this means that (a) either the projection did a bad job (the island does not actually exist in the high-dimensional space *D*); or (b) the island actually exist in *D*, *i.e.*, there are very similar samples that get assigned different labels. Refining (b), this further indicates that (b1) the classifier did a good job for a complex configuration in the data space *D*, or (b2) the classifier misclassified the point(s) in the island for some reason. To understand which of these cases actually occur, we plot misclassified points atop the dense map as half-transparent white disks. Hence, regions having many (densely packed) misclassifications show up as white areas. Figure 5 shows this for the LR and CNN classifiers, all projections. The insets (t-SNE dense map) exemplify how islands point to two of the above-mentioned issues: In Fig. 4a, we see two very small color islands around the misclassified samples *A* and *B*. These islands indicate the extent up to which other samples, close to *A* or *B*, would also get misclassified. In contrast, the detail in Fig. 4b shows a (red) island containing no white dots (misclassifications). This island either reflects a real small-scale)variation of the classifier decision, or else reflects an artifact of the t-SNE projection.

Separately, we see that, overall, the LR dense maps have more white dots than the CNN ones, which correlates with the lower LR accuracy (Tab. 1). More interestingly, we see that the white points are *non-uniformly* spread over the dense maps by different projections. MDS and PLMP show many islands without white dots, which indicate that these projections have trouble preserving *n*D similarities in 2D. At the other extreme, t-

SNE, and evenmore so UMAP, strongly pack the white dots, which tells that misclassifications actually occur for quite similar data samples. These two dense maps effectively show the *confusion zones* to the ML specialist, so one can use them to decide which kinds of samples need to be further added to the training set to improve accuracy.

5 DISCUSSION

We discuss next a few key aspects of our evaluation.

Best choice: From all our experiments, t-SNE and UMAP appear to be the best projections for constructing dense maps in terms of recognizability of decision boundaries in the produced patterns, limited errors (spurious islands), and concentration of confusion zones (misclassifications). Since UMAP has similar properties with t-SNE but is significantly faster, we label it as the optimal candidate for this task.

Influence factors: As mentioned, dense maps depend not only on the direct projection *P* but also on its inverse P^{-1}. We studied in detail the dependency on *P*, but only used a single P^{-1} implementation (iLAMP). This is due to the fact that we are not aware of any other scalable, generic, and publicly-available inverse projection alternative. However, designing such alternatives is an interesting topic in itself for future work.

Experiment coverage: Dense maps constructed using projections are a novel technique in high-dimensional visualization. Besides their use discussed here for showing classifier boundaries, they are also used to analyze projection quality (Martins et al., 2014; Aupetit, 2007). All such maps strongly depend on the projection technique being used. To our knowledge, our current work that evaluates how dense maps depend on the choice of 28 possible projection techniques, is the broadest evaluation of this type in existence. To limit the amount of work required to analyze over hundred classifier-projection combinations, we designed a two-phase experiment where we pre-select the best projections (using a simple classification problem) to study next in detail. This, of course, limits the potentially interesting insights one can find. The same is true for our choice of using a single (though, highly-recognized complex ML benchmark) dataset.

Replicability and extensibility: To be useful, our work on evaluating projection-based dense maps must be accessible, replicable, and extensible. All involved materials and methods (projections, datasets, dense maps, classifiers, automated workflow scripts) are available online (Espadoto et al., 2018). We intend to organically extend this repository with new instances along all above-mentioned dimensions.
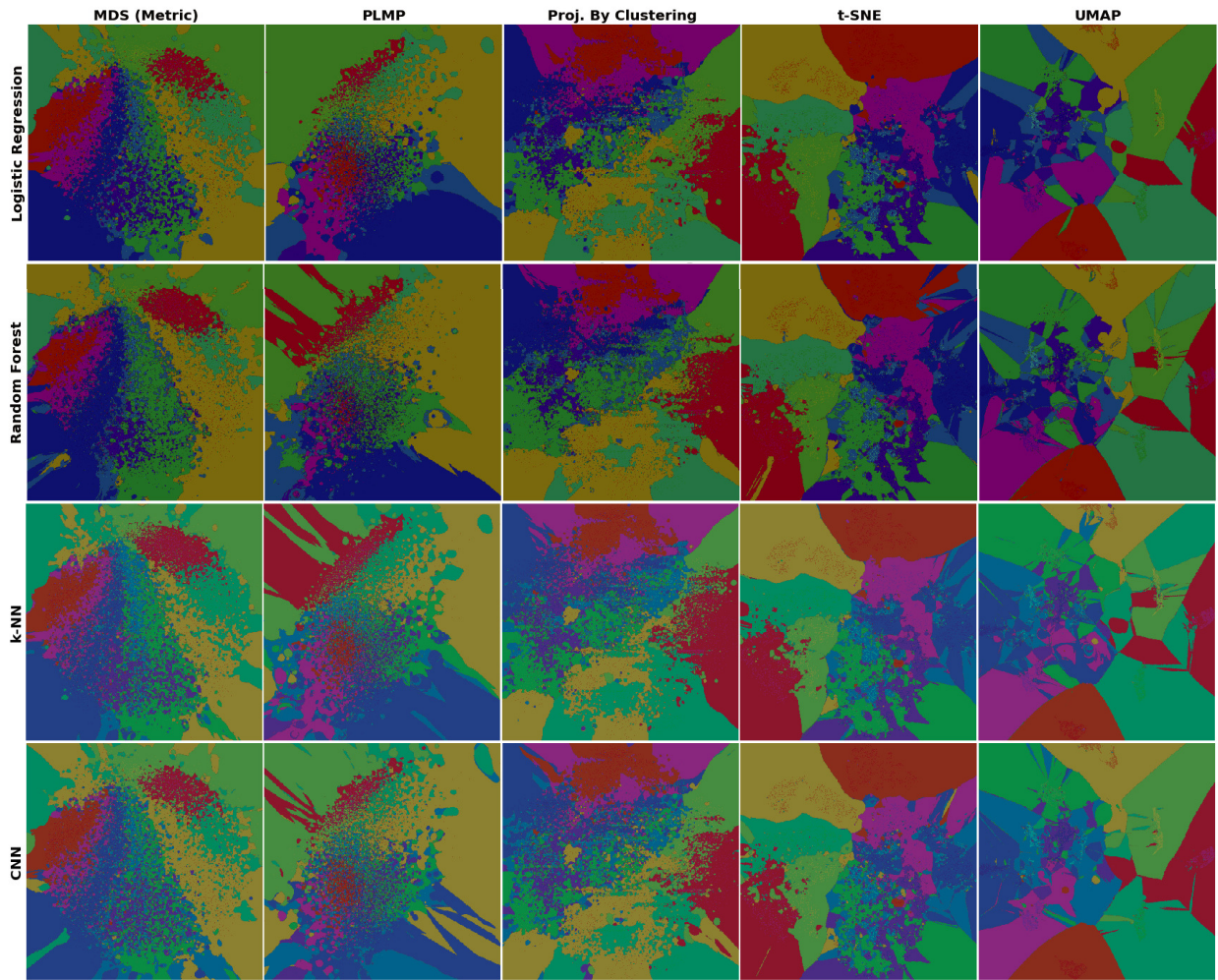
Figure 4: Dense maps for all classifiers, 10-class dataset, five best-performing projections.
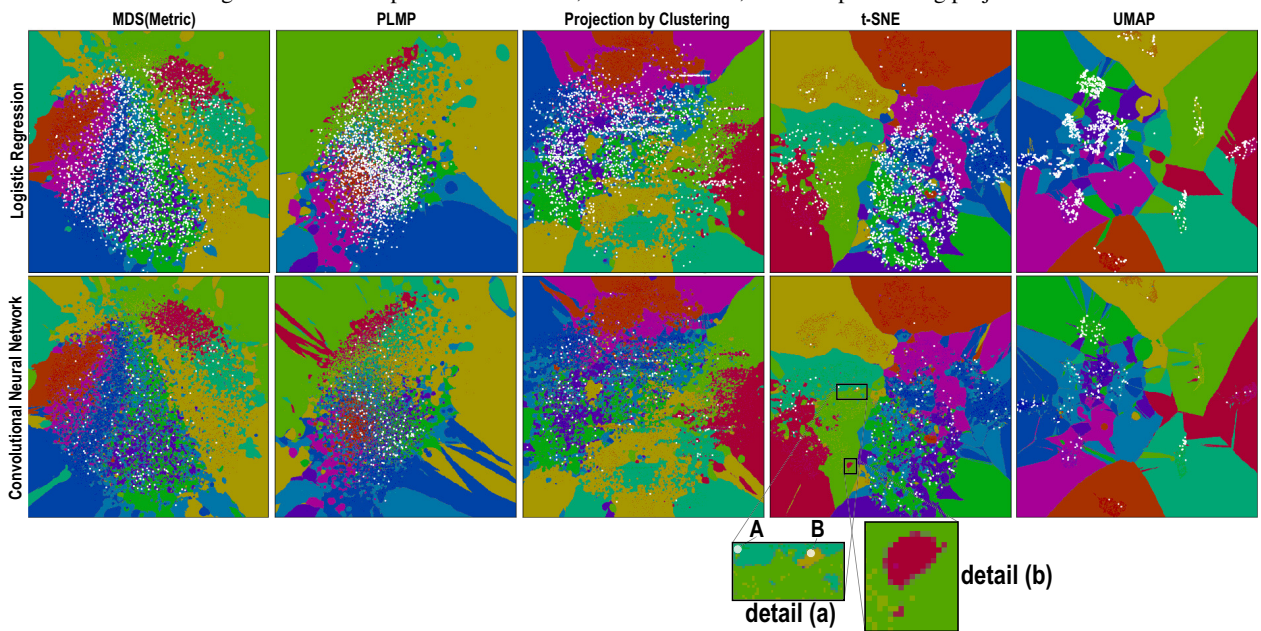

Figure 5: Classification errors (white dots) shown atop of the dense maps, LR and CNN classifiers.

6 CONCLUSIONS

In this paper we have presented a methodology for evaluating the quality of multidimensional projections for the task of constructing 2D dense maps to visualize decision boundaries of ML classifiers. To this end, we have evaluated 28 well-known projections on a two-class, respectively ten-class, subset of a well-known ML benchmark, using four classifiers often used in practice. Our evaluation shows wide, and to our knowledge, not yet known, differences between the behavior of the studied projections. Using a visual analytics methodology, we next refined our analysis to a small set of five high-quality projections, and found that t-SNE and UMAP perform best for this task. On the practical side, our results can be used to drive the selection of suitable projections for other types of dense maps used in high-dimensional visualization. On the methodological side, our workflow can serve as a model for the exploration of a large design space in similar visual analytics contexts.

Future work can address several directions. First, we aim to explore how dense maps depend on the inverse projection, and propose better alternatives to iLAMP. Secondly, we aim to detect, flag, and possibly eliminate projection errors, like spurious islands, so as to make the dense map interpretation simpler and faster. Last but not least, we will extend our publicly available results (data, code, workflow scripts) and hope thereby to create the starting point for a recognized benchmark for the practical analysis of the quality of multidimensional projections.

ACKNOWLEDGEMENTS

REFERENCES

Amorim, E., Brazil, E., Daniels, J., Joia, P., Nonato, L., and Sousa, M. (2012). iLAMP: Exploring high-dimensional spacing through backward multidimensional projection. In *Proc. IEEE VAST*.

Aupetit, M. (2007). Visualizing distortions and recovering topology in continuous projection techniques. *Neurocomputing*, 10(7-9):1304–1330.

Belkin, M. and Niyogi, P. (2002). Laplacian eigenmaps and spectral techniques for embedding and clustering. In *Advances in Neural Information Processing Systems (NIPS)*, pages 585–591.

Chen, Y., Crawford, M., and Ghosh, J. (2006). Improved nonlinear manifold learning for land cover classification via intelligent landmark selection. In *Proc. IEEE IGARSS*, pages 545–548.

Dasgupta, S. (2000). Experiments with random projection. In *Proc. of the Sixteenth conference on Uncertainty in artificial intelligence*, pages 143–151. Morgan Kaufmann.

Donoho, D. L. and Grimes, C. (2003). Hessian eigenmaps: Locally linear embedding techniques for high-dimensional data. *Proceedings of the National Academy of Sciences*, 100(10):5591–5596.

Espadoto, M., Rodrigues, F. C. M., and Telea, A. C. (2018). Projection-based dense map evaluation. http://snip.li/8pa.

Faloutsos, C. and Lin, K. (1995). FastMap: A fast algorithm for indexing, data-mining and visualization of traditional and multimedia datasets. *ACM SIGMOD Newsletter*, 24(2):163–174.

Féraud, R. and Clérot, F. (2002). A methodology to explain neural network classification. *Neural Networks*, 15(2):237–246.

Hamel, L. (2006). Visualization of support vector machines with unsupervised learning. In *Proc. Computational Intelligence and Bioinformatics and Computational Biology (CIBCB)*. IEEE.

Hoffman, P. and Grinstein, G. (2002). A survey of visualizations for high-dimensional data mining. In Fayyad, U., Grinstein, G., and Wierse, A., editors, *Proc. Information Visualization in Data Mining and Knowledge Discovery*, pages 47–82. Morgan Kaufmann.

Hyvarinen, A. (1999). Fast ICA for noisy data using gaussian moments. In *Proc. IEEE ISCAS*, volume 5, pages 57–61.

Joia, P., Coimbra, D., Cuminato, J. A., Paulovich, F. V., and Nonato, L. G. (2011). Local affine multidimensional projection. *IEEE TVCG*, 17(12):2563–2571.

Jolliffe, I. T. (1986). Principal Component Analysis and Factor Analysis. In *Principal component analysis*, pages 115–128. Springer.

Kingma, D. P. and Ba, J. (2014). Adam: A method for stochastic optimization. *arXiv:1412.6980v9 [cs.LG]*.

Krizhevsky, A., Sutskever, I., and Hinton, G. (2012). Imagenet classification with deep convolutional neural networks. In *Advances in Neural Information Processing Systems (NIPS)*, pages 1097–1105.

Kruskal, J. B. (1964). Multidimensional scaling by optimizing goodness of fit to a nonmetric hypothesis. *Psychometrika*, 29(1):1–27.

LeCun, Y. and Cortes, C. (2018). MNIST handwritten digits dataset. http://yann.lecun.com/exdb/mnist.

Liu, S., Maljovec, D., Wang, B., Bremer, P.-T., and Pascucci, V. (2015). Visualizing high-dimensional data: Advances in the past decade. *IEEE TVCG*, 23(3):1249–1268.

Manning, C. D., Schütze, H., and Raghavan, P. (2008). *Introduction to Information Retrieval*, volume 39. Cambridge University Press.

Martins, R., Coimbra, D., Minghim, R., and Telea, A. (2014). Visual analysis of dimensionality reduction quality for parameterized projections. *Computers & Graphics*, 41:26–42.

McInnes, L. and Healy, J. (2018). UMAP: Uniform Manifold Approximation and Projection for Dimension Reduction. *arXiv:1802.03426v1 [stat.ML]*.

Migut, M. A., Worring, M., and Veenman, C. J. (2015). Visualizing multi-dimensional decision boundaries in 2D. *Data Mining and Knowledge Discovery*, 29(1):273–295.

Minghim, R., Paulovich, F. V., and Lopes, A. A. (2006). Content-based text mapping using multi-dimensional projections for exploration of document collections. In *Proc. SPIE*, volume 6060. Intl. Society for Optics and Photonics.

Nonato, L. and Aupetit, M. (2018). Multidimensional projection for visual analytics: Linking techniques with distortions, tasks, and layout enrichment. *IEEE TVCG*. DOI:10.1109/TVCG.2018.2846735.

Paulovich, F. V., Eler, D. M., Poco, J., , Botha, C. P., Minghim, R., and Nonato, L. G. (2011). Piecewise laplacian-based projection for interactive data exploration and organization. *Computer Graphics Forum*, 30(3):1091–1100.

Paulovich, F. V. and Minghim, R. (2006). Text map explorer: a tool to create and explore document maps. In *Proc. Intl. Conference on Information Visualisation (IV)*, pages 245–251. IEEE.

Paulovich, F. V., Silva, C. T., and Nonato, L. G. (2010). Two-phase mapping for projecting massive data sets. *IEEE TVCG*, 16(6):1281–1290.

Pekalska, E., de Ridder, D., Duin, R. P. W., and Kraaijveld, M. A. (1999). A new method of generalizing Sammon mapping with application to algorithm speed-up. In *Proc. ASCI*, volume 99, pages 221–228.

Rauber, P. E., Fadel, S. G., Falcao, A. X., and Telea, A. C. (2017a). Visualizing the hidden activity of artificial neural networks. *IEEE TVCG*, 23(1):101–110.

Rauber, P. E., Falcão, A. X., and Telea, A. C. (2017b). Projections as visual aids for classification system design. *Information Visualization*, 17(4):282–305.

Ribeiro, M. T., Singh, S., and Guestrin, C. (2016). Why should I trust you?: Explaining the predictions of any classifier. In *Proc. ACM SIGMOD KDD*, pages 1135–1144.

Rodrigues, F. C. M., Hirata Jr, R., and Telea, A. C. (2018). Image-based visualization of classifier decision boundaries. In *Proc. SIBGRAPI*. in press.

Roweis, S. T. and Saul, L. L. K. (2000). Nonlinear dimensionality reduction by locally linear embedding. *Science*, 290(5500):2323–2326.

Schölkopf, B., Smola, A., and Müller, K. (1997). Kernel principal component analysis. In *Proc. International Conference on Artificial Neural Networks*, pages 583–588. Springer.

Sorzano, C., Vargas, J., and Pascual-Montano, A. (2014). A survey of dimensionality reduction techniques. arXiv:1403.2877 [stat.ML].

Tenenbaum, J. B., Silva, V. D., and Langford, J. C. (2000). A global geometric framework for nonlinear dimensionality reduction. *Science*, 290(5500):2319–2323.

van der Maaten, L. and Hinton, G. (2008). Visualizing data using t-SNE. *JMLR*, 9(Nov):2579–2605.

van der Maaten, L. and Postma, E. (2009). Dimensionality reduction: A comparative review. Tech. report TiCC TR 2009-005, Tilburg University, Netherlands.

Xiao, H., Rasul, K., and Vollgraf, R. (2017). Fashion-MNIST: A Novel Image Dataset for Benchmarking Machine Learning Algorithms. arXiv:1708.07747v2 [cs.LG].

Zhang, Z. and Wang, J. (2007). MLLE: Modified locally linear embedding using multiple weights. In *Advances in Neural Information Processing Systems (NIPS)*, pages 1593–1600.

Zhang, Z. and Zha, H. (2004). Principal manifolds and nonlinear dimensionality reduction via tangent space alignment. *SIAM Journal on Scientific Computing*, 26(1):313–338.

Zou, H., Hastie, T., and Tibshirani, R. (2006). Sparse principal component analysis. *Journal of Computational and Graphical Statistics*, 15(2):265–286.

APPENDIX: PROJECTION PARAMETERS

Table 3: Parameters used for each projection.

Projection	Parameters
Factor Analysis	iter: 1000
FastICA	fun: exp, iter: 200
Fastmap	default parameters
IDMAP	default parameters
Isomap	neighbors: 7, iter: 100
Kernel PCA (Linear)	default parameters
Kernel PCA (Polynomial)	degree: 2
Kernel PCA (RBF)	default parameters
Kernel PCA (Sigmoid)	default parameters
LAMP	iter: 100, delta: 8.0
Landmark Isomap	neighbors: 8
Laplacian Eigenmaps	default parameters
LLE	neighbors: 7, iter: 100
LLE (Hessian)	neighbors: 7, iter: 100
LLE (Modified)	neighbors: 7, iter: 100
LTSA	neighbors: 7, iter: 100
MDS (Metric)	init: 4, iter: 300
MDS (Non-Metric)	init: 4, iter: 300
PCA	default parameters
PLMP	default parameters
PLSP	default parameters
Projection By Clustering	default parameters
Random Projection (Gaussian)	default parameters
Random Projection (Sparse)	default parameters
Rapid Sammon	default parameters
Sparse PCA	iter: 1000
t-SNE	perplexity: 20, iter: 3000
UMAP	neighbors: 10